

# Are EEG functional networks really describing the brain? A comparison with other information-processing complex systems

Sofia Gil-Rodrigo,<sup>1</sup> Raúl López-Martín,<sup>2</sup> Görsev Yener,<sup>3</sup> Jan R. Wiersema,<sup>4</sup> Bahar Güntekin,<sup>5</sup> and Massimiliano Zanin<sup>2,\*</sup>

<sup>1</sup>*Center for Brain and Cognition, Department and School of Engineering, Universitat Pompeu Fabra, Barcelona, Spain*

<sup>2</sup>*Instituto de Física Interdisciplinar y Sistemas Complejos IFISC (CSIC-UIB), Campus UIB, 07122 Palma de Mallorca, Spain*

<sup>3</sup>*Izmir University of Economics, Faculty of Medicine, Izmir, Turkey*

<sup>4</sup>*Department of Experimental Clinical and Health Psychology, Ghent University, Ghent, Belgium*

<sup>5</sup>*Department of Biophysics, School of Medicine, Istanbul Medipol University, Istanbul, 34810, Turkey*

Functional networks representing human brain dynamics have become a standard tool in neuroscience, providing an accessible way of depicting the computation performed by the brain in healthy and pathological conditions. Yet, these networks share multiple characteristics with those representing other natural and man-made complex systems, leading to the question of whether they are actually capturing the uniqueness of the human brain. By resorting to a large set of data representing multiple financial, technological, social, and natural complex systems, and by relying on Deep Learning classification models, we show how they are highly similar. We specifically reach the conclusion that, under some general reconstruction methodological choices, it is as difficult to understand whether a network represents a human brain or a financial market, as to diagnose a major pathology. This suggests that functional networks are describing information processing mechanisms that are common across complex systems; but that are not currently defining the uniqueness of the human mind. We discuss the consequence of these findings for neuroscience and complexity science in general, and suggest future avenues for exploring this interesting topic.

One of the most promising ways of representing the flow of information in a complex system is provided by functional complex networks, and, not surprisingly, these have strongly impacted neuroscience in the last decade. Beyond illustrating the structures created by information processing in healthy and pathological conditions [1, 2], functional brain networks have also been found to share many topological characteristics with similar network representations of other complex systems. As already highlighted in Ref. [3], both brain and financial networks are non-random, small-world, modular and hierarchical. This, on the one hand, can be explained by the fact that both systems are the results of similar processes, i.e. investors communicate and compute information in a way akin to neurons [4]. Yet, on the other hand, this may also be the result of the default approach of understanding the brain via metaphors, hence via similarities with other systems. Since early times, understanding the brain was fuelled by metaphors corresponding to technical and technological systems that were at that time possessed and thought to be understood [5, 6]. To illustrate, Aristotle thought of the brain as a blood cooling machine; Descartes saw the brain as a hydraulic system; further metaphors included the clock, electricity, the telegraph, and computers - including working memory, information processing, computational capabilities, and so on. More recently the brain is understood as a network, not surprisingly, as our societies are built on top of networked systems [7]. In other words, the history of neuroscience has been the history of these metaphors. This metaphor-based approach has shown its value, but is also limited by construction, as it cannot give us more insights than what we know about the metaphor. We may be able to find useful similarities but it will not reveal the uniqueness (and complexity) of the system under study, in this case, of the human brain.

The human brain is not like any other complex system; on the contrary, it is the only system we know of that displays authentic intelligence, is self-aware, and is even able to write, read, and understand a scientific paper. This fact leads to two major questions. Firstly, how much are functional brain networks really representative of the human brain dynamics, as opposed to the general dynamics of information-processing complex systems. Secondly, and consequence of this, how representative are these networks of alterations emerging in pathologies. In other words, while Aristotle could only leverage limited tools and had to use a hypothesis driven/top down approach, nowadays we do have other possibilities, and we specifically can apply strong bottom up/data driven approaches to detect unique features and characteristics not present in other complex systems.

Unfold such new approach in the context of brain functional networks requires facing two methodological problems. Firstly, an unbiased and non-parametric way of analysing and comparing functional networks is needed. To illustrate, observing no differences in a given topological metric only indicates that such specific property is similar, but differences affecting other topological aspects cannot be excluded. In other words, a complete analysis would require testing all possible (both known and yet to be proposed) topological metrics [8]. Secondly, the result of reconstructing functional

---

\* Corresponding author: massimiliano.zanin@gmail.com

networks strongly depends on the parameter used throughout the process, for which in many cases there are no theoretical guidelines, and whose values are left to the practitioner’s judgement [9].

We here address these two problems by, on the one hand, using Deep Learning models to assess how similar two sets of functional networks are, i.e. whether or not there are structural elements supporting their differentiation. DL models are hypotheses-free by construction, as they build a tailored abstract representation of the data. On the other hand, we guide the reconstruction of functional brain networks through their capacity of discriminating between healthy subjects and patients suffering from Parkinson’s Disease (PD). These networks will then be compared against the functional representations of other complex systems, here drawn from financial, technological, social, and natural ones. In other words, considered brain functional networks are not tailored to this problem, but are rather optimised according to a typical neuroscience question. We finally pose the question: are we really capturing the uniqueness of the human brain?

## RESULTS

We start by reconstructing functional networks representing brain dynamics of control subjects and PD patients, from resting state EEG recordings (Materials and Methods, SI Appendix I.A). For each subject and group, short segments of length  $l$  of EEG time series are extracted, and a functional network is reconstructed therefrom using four different synchronisation measures (Materials and Methods). We further consider two possibilities: unweighted networks, where links are binarised according to a threshold  $\tau$ ; and weighted ones, in which links are deleted if their weight is below  $\tau$ , but whose weight is preserved if passing this filter. Two sets of 500 functional networks (one set per group, for a total of  $10^3$  networks) are then used to train a Graph Isomorphism Network (GIN) DL model [10] (Materials and Methods), which is then evaluated over two independent (but similarly constructed) sets of networks. The result, measured in terms of the median classification accuracy over 500 independent realisations, indicates whether the two sets are structurally similar, or, on the contrary, present some unique and characteristic structures.

The evolution of the accuracy as a function of  $\tau$ ,  $l$ , and the synchronisation measure, is reported in Fig. 1 a) and b) for unweighted networks. As the objective is to use the best network representation to discriminate the two conditions, we set  $\tau = 0.2$ ,  $l = 1,400$ , and Rank Correlation in subsequent analyses of unweighted networks. Note that filtering the data in specific frequency bands does not improve the discrimination (SI Appendix II.A). A similar analysis is performed for the weighted case, using the previously obtained segment length of  $l = 1,400$ , obtaining a maximum discrimination capability for  $\tau = 0.3$  and Rank Correlation - see Fig. 1 c).

Using these networks as a reference, we then move to the analysis of financial markets (SI Appendix I.B-C, Materials and Methods), with the aim of finding the functional networks representation that minimise the classification score when compared with the brain ones. In other words, we probe whether financial functional networks can be constructed to be as similar as possible to the dynamics observed in the brain. Panels d) and f) of Fig. 1 report the evolution of the classification score for respectively unweighted and weighted networks, as a function of the threshold, segment lengths and synchronisation metric. Very low classification scores can be obtained, especially in the case of the unweighted versions of the networks, even below 0.6. Similar analyses are reported in panels e) and g) for other complex systems (Materials and Methods, SI Appendix I.D-F). A synthesis of the best parameter sets is included in SI Appendix IV.D.

The synthesis of these results, see Fig. 2, highlights a key point. The similarity of functional networks of multiple complex systems to those representing brain activity of healthy individuals is on average the same as the similarity between the latter ones and those of PD patients. Most notably, the best case can be found for unweighted Forex networks, for which the classification score drops to 0.6 - as opposed to the 0.75 reported in Fig. 1 a) and b). In other words: there are more differences between control subjects and Parkinson’s patients, than between the same control subjects and the Forex market. This is not a side effect of using a DL classification model; an analysis of the topological metrics of both sets of networks confirms their similarity (SI Appendix V.C), with structures characterised by a core-periphery configuration, and by a high frequency of 3- and 4-nodes complete motifs (SI Appendix V.D). The reduced differences across complex systems is also not due to a lack in sensitivity of the DL model (SI Appendix VI). The similarity between EEG and Forex networks can additionally be increased by performing a downsampling of the time series of the latter (SI Appendix VII), suggesting the presence of specific time scales in which similar computations may be performed by both systems. Note that a similar processing does not yield any benefit in the case of winds’ networks (SI Appendix VII); and is further pointless in the other data sets, due to their lower time resolution.

The previous results have been obtained by carefully tuning the parameters of the reconstruction process (i.e.  $\tau$  and  $l$ ) to yield networks as similar as possible to those representing brain dynamics. In order to explore how generalisable these results are, we firstly analyse networks representing other financial markets when these are reconstructed using the same  $\tau$  and  $l$  as optimised for the S&P 500 data set. Results (see from DJI to STI in Fig. 2, and SI Appendix

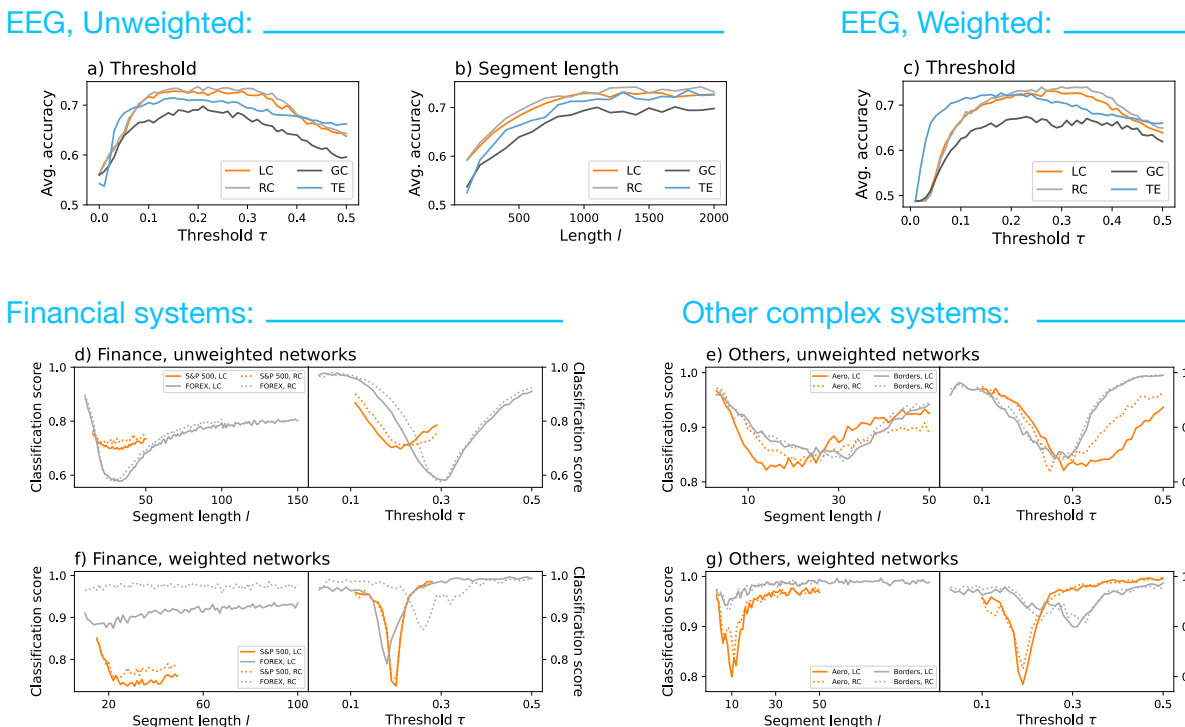


FIG. 1. Optimising the reconstruction of functional networks. a)-b) Classification score between unweighted functional networks of control subjects and PD patients, as a function of the threshold  $\tau$ , the segment length  $l$ , and the synchronisation metric (line colours, see legends, and Materials and Methods for details). c) Classification results for EEG weighted functional networks, as a function of the threshold  $\tau$  and the synchronisation metric ( $l = 1400$ ). d)-g) Classification score between brain functional networks of control subjects, and functional networks of other complex systems, both unweighted (top panels) and weighted (bottom panels), as a function of the segment length  $l$  and the threshold  $\tau$ .

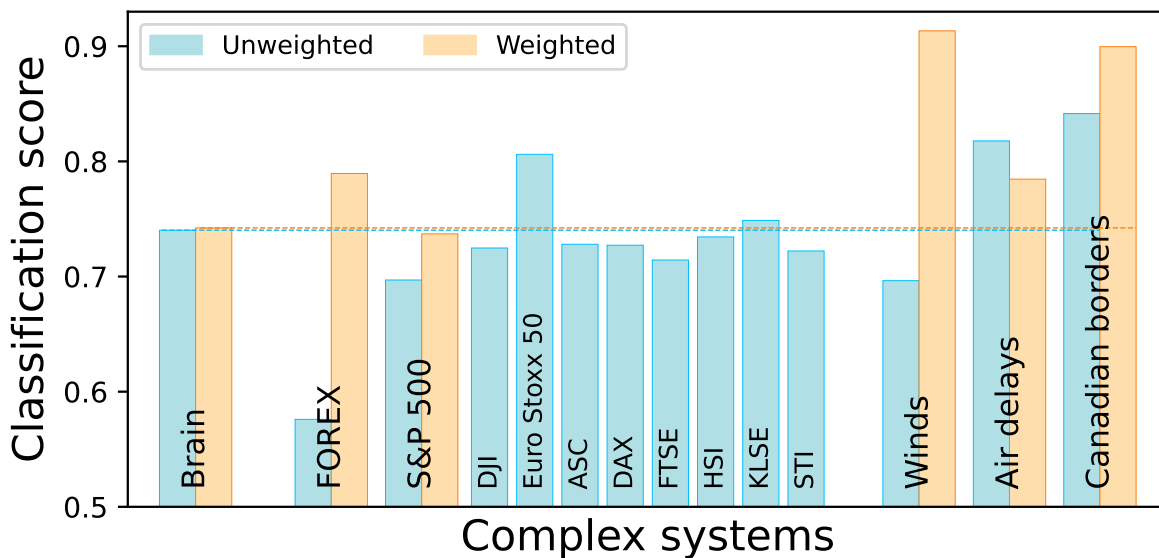


FIG. 2. Synthesis of the best classification scores obtained across different complex systems. Blue and orange bars respectively correspond to results for unweighted and weighted network classifications. The two leftmost bars correspond to the classification between control subjects and PD patients, as in Fig. 1 b) and c); for convenience, these reference levels are marked with two horizontal lines.

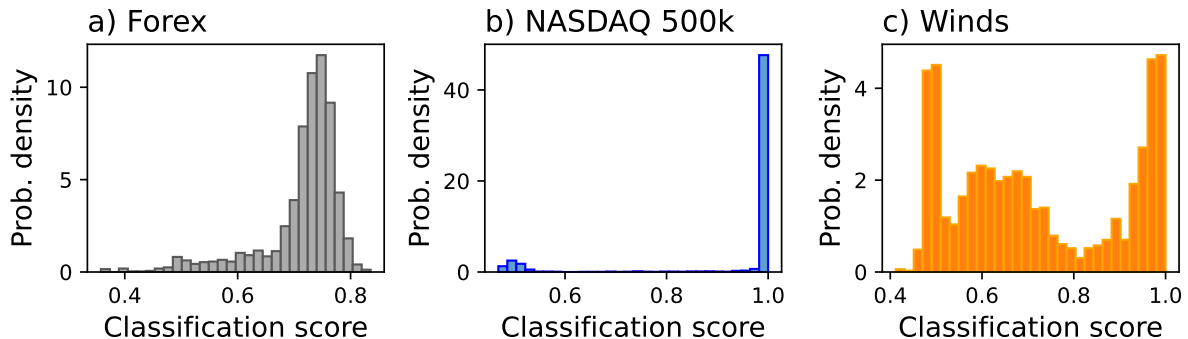


FIG. 3. Analysis of extended data sets. The three panels report the probability density function of the classification score obtained when considered extended data sets for a) Forex, b) NASDAQ 500k, and c) winds data. See SI Appendix I for complete data set descriptions.

IV.A) suggest no major increase in identifiability. In other words, all markets here considered have a similar structure that is resilient to the reconstruction procedure, and that is independent from main market characteristics (see SI Appendix V.A). We further analyse three data sets (Forex, NASDAQ 500k, and winds' data) for which we have access to a larger set of time series. Specifically, instead of selecting 30 nodes according to some criteria, we sampled a large number of sets of 30 randomly-chosen time series, and reconstructed the corresponding functional networks according to the optimised parameters used in Fig. 2. Results reported in Fig. 3 indicates that Forex and winds' data maintain a similar identifiability, with the latter case being weakly correlated to the spatial location of sensors (see SI Appendix V.B). On the other hand, NASDAQ 500k networks becomes highly identifiable; this is probably due to the inclusion of stocks of low market capitalisation, which may have a highly heterogeneous dynamics.

## DISCUSSION AND CONCLUSIONS

Functional networks representing brain dynamics, and the dynamics of other complex systems, in many cases share similar structures. These similarities are highlighted by the difficulties encountered by state-of-the-art DL models to discriminate them, suggesting a low identifiability [11]; and are further confirmed by comparable topological metrics, as previously highlighted in other works [3]. Differences are in many cases, and especially in the case of financial networks, of the same magnitude as the differences between functional networks of control subjects and patients suffering from PD. In other words: it is as complex to discriminate between the two conditions, as to recognise whether one of these networks actually represents a human brain or a financial market.

This surprising result generates many interesting research questions. First of all, where does this similarity come from? Is it a consequence of the way of reconstructing functional networks, or even of the concept of functional network itself? Or is rather a consequence of representing structures that are universal in information-processing systems? The fact that the maximum similarity is obtained for Forex networks, i.e. possibly the most complex and interconnected financial market, and is minimal in the Canadian borders data set, where a computation between travellers is actually not expected to exist, supports (but does not causally prove) the latter option. The relatively low identifiability of PD networks also supports this idea: while patients have an impaired cognition, this does not mean that no computation at all is performed by their brains; differences may therefore only stem from how altered such computation is. In other words, functional networks may only be the last step in the use of metaphors in neuroscience.

As a second question, given that brains and financial markets are very difficult to distinguish, are these functional networks really representing the uniqueness of the human brain? While the answer seems to be negative, this does not diminish the usefulness of functional networks in a neuroscience context. As widely shown in the literature, these can be used to elucidate information flows in the brain, both at rest and during cognitive tasks; and can further be used to detect pathological conditions. Yet, results here reported suggest (but, yet again, do not prove) that the resulting networks are not describing the uniqueness of the human brain, but rather common features of information-processing systems.

Thirdly, if the previous conjecture is true, a more complex (and even philosophical in nature) question remains: can functional networks be reconstructed, aimed at representing what is unique to the human brain? I.e., representing not only computation, but even our unique self-awareness and the theory of mind [12–15]?

While the present work relies on state-of-the-art methods, especially regarding the assessment of the similarities

between networks, it is clearly not free of limitations. On one hand, only one set of control subjects and one set of patients have been considered. Generalisability could be confirmed by using additional EEG recordings; and the inclusion of different brain pathologies of different degrees of severity, and of neurodivergent groups such as autism or attention deficit hyperactivity disorder, may shed light on when (if at all) the computation capability is reduced. The considered EEG data set comprises recording for only 30 electrodes, and it may be suspected that this coarse-graining of brain dynamics may mask important local structures. In other words, low classification scores may be the result of a “curse of dimensionality”. Yet, this would not be compatible with the high scores observed for air delays and Canadian borders’ data sets. Time scales have shown to be an important element (see SI Appendix VII); data for complex systems of faster evolution, or even higher resolution data for those here considered, may improve our understanding of the previously posed questions. Finally, while GINs are the current state-of-the-art in DL models for classifying groups of networks, machine learning and artificial intelligence are fast evolving fields; better and more efficient solutions may appear in the near future. In order to support the scientific community in this last point, we include with this work a set of networks representing the worst obtained classification between control subjects and Forex, which can be used as benchmark in future studies (see SI Appendix VIII).

In conclusion, in this work we have leveraged DL models to highlight the similarities between functional networks representing human brain dynamics, and the dynamics of other complex systems. Presented results lead to an essential question: are functional networks really capturing the essence of human brain dynamics, or only patterns common to all information-processing systems? Furthermore, in the latter case, can we rely on functional networks to probe the dynamics of the human brain, with the hope of obtaining diagnostic and therapeutic knowledge? In other words: how can findings about the uniqueness of human brain impact our understanding (and hence diagnostics, support, and therapeutics) of neurodivergence and neuropathology? While the analyses here presented do not yield a conclusive answer, they surely highlight the necessity of delving deeper in our understanding of this essential tool.

#### ACKNOWLEDGMENTS

This project has received funding from the European Research Council (ERC) under the European Union’s Horizon 2020 research and innovation programme (grant agreement No 851255). This work was partially supported by Grant CNS2023-144775 funded by MICIU/AEI/10.13039/501100011033 by “European Union NextGenerationEU/PRTR”, and by the María de Maeztu project CEX2021-001164-M funded by the MICIU/AEI/10.13039/501100011033 and FEDER, EU.

## MATERIALS AND METHODS

### Data sets

We consider a large number of data sets representing the dynamics of human brain in normal and pathological (Parkinson’s Disease) condition; and of other complex systems, spanning financial, technological, and social systems. These include:

- Financial markets: Forex, i.e. the market for the trading of currencies; stocks composing the US S&P 500 and DJI indices; stocks composing the European Euro Stoxx 50 index; companies classified as aggressive small caps (ASM) in the US NYSE stock exchange; and companies composing several national indices, including the German DAX, UK FTSE, Hong Kong’s HSI, Malaysian’s KLSE, and the Singaporean STI.
- Wind speed information recorded throughout the main European airports.
- Information about delays in major European airports.
- Daily number of foreign visitors entering Canada.

A full list of them, and of the elements thereof composed, is provided in SI Appendix I. Additionally, a description of the pre-processing carried out in each case is reported in SI Appendix II.

### Functional network reconstruction

Given a set of 30 time series (as this is the number of available EEG electrodes), segments of length  $l$  are extracted at random from them, and the weight of links between pairs of them is obtained using four standard metrics: linear correlation (LC), rank correlation (RC), Granger Causality (GC) [16], and Transfer Entropy (TE) [17, 18] - see SI Appendix III for definitions. In the case of GC and TE,  $p$ -values are rescaled to yield values similar to those of LC and RC. Finally, two variants of networks are obtained: unweighted ones, in which all links with weight below a threshold  $\tau$  are discarded, and the weight of surviving links is set to one; and weighted ones, in which the weight of links greater than  $\tau$  is preserved - see SI Appendix III.

### Deep Learning model and classification

The Deep Learning model used for the network classification is the Graph Isomorphism Neural Network (GIN) [10], which is as powerful as the Weisfeiler-Lehman test regarding graph classification, enabling it to capture the concept of isomorphism [10]. This makes it the most suitable tool for classifying networks based on their topology without introducing biases derived from focusing on specific arbitrary topological metrics. The GIN model was implemented using the Python *Pytorch* library [19] and its structure consists of three convolutional layers of dimension  $(h, h)$  and two fully connected layers of size  $3h$ , where  $h = 32$ .

The classification process began with the random selection of 500 networks from each of the two classes. Using a batch size of 64 networks and running for 5,000 epochs, we performed 500 classifications for each reconstruction parameter value, averaging the results to generate the curves shown in Fig. 1.

Initially, we classified control brain networks against PDs brain networks (see Fig. 1 (a-c)). For subsequent classifications of control brain networks against other complex systems, we maintained the optimal  $l$  and  $\tau$  that provided the best accuracy in distinguishing control subjects from PD. This approach assumes that the most effective representation in differentiating control and Parkinson’s brain networks is also the best representation of a healthy brain. We then swept these parameters for the networks of the other class to obtain the remaining curves observed in Fig. 1. Further details are reported case by case in SI Appendix IV, and a synthesis of the best parameters can be found in SI Appendix IV.D.

## I. DATA SOURCES

### A. EEG data

Data set to be described.

### B. Stock markets' data

Four different data sets representing the dynamics of stock markets have been considered, specifically:

- The 30 largest companies, in terms of market capitalisation, composing the **S&P 500** (Standard and Poor's 500) index. Analysed data correspond to the time period from February 1<sup>st</sup> 2013 to February 2<sup>nd</sup> 2024, for a total of 2,790 data points. The full list is reported in Tab. I.
- The 30 largest companies, in terms of market capitalisation, composing the German **DAX** (Deutscher Aktienindex) index. Analysed data correspond to the time period from September 30<sup>th</sup> 2022 to April 30<sup>th</sup> 2024, for a total of 403 data points. The full list is reported in Tab. II.
- The 30 largest companies classified as **aggressive small caps (ASM)** in the NYSE stock exchange. These are defined as companies of small capitalisation (below \$2 billion USD) and with an increase in the EPS (earnings per share) in the last year greater than 25%. Analysed data correspond to the time period from December 16<sup>th</sup> 2020 to May 1<sup>st</sup> 2024, for a total of 847 data points. The full list is reported in Tab. III.
- The 30 largest companies, in terms of market capitalisation, composing the UK **FTSE 100** (Financial Times Stock Exchange 100 Index) index. Analysed data correspond to the time period from July 18<sup>th</sup> 2022 to May 1<sup>st</sup> 2024, for a total of 451 data points. The full list is reported in Tab. IV.
- The 30 largest companies, in terms of market capitalisation, composing the European **Euro Stoxx 50** index. Analysed data correspond to the time period from September 3<sup>rd</sup> 2001 to February 2<sup>nd</sup> 2024, for a total of 5,710 data points. The full list is reported in Tab. IV.
- The 30 largest companies, in terms of market capitalisation, composing the **Dow Jones Industrial Average (DJI)** index. Analysed data correspond to the time period from March 20<sup>th</sup> 2019 to February 2<sup>nd</sup> 2024, for a total of 1,227 data points. The full list is reported in Tab. VI.
- The 30 largest companies, in terms of market capitalisation, composing the Hong Kong's **Hang Seng (HSI)** index. Analysed data correspond to the time period from December 23<sup>rd</sup> 2020 to April 30<sup>th</sup> 2024, for a total of 882 data points. The full list is reported in Tab. VII.
- The 30 largest companies, in terms of market capitalisation, composing the Malaysian's **FTSE Bursa Malaysia (KLSE)** index. Analysed data correspond to the time period from October 26<sup>th</sup> 2020 to April 30<sup>th</sup> 2024, for a total of 852 data points. The full list is reported in Tab. VIII.
- The 30 companies composing the **Straight Times (STI)** index, representing the largest companies in the Singapore Exchange market. Analysed data correspond to the time period from July 14<sup>th</sup> 2022 to April 30<sup>th</sup> 2024, for a total of 450 data points. The full list is reported in Tab. IX.

In all cases, data have been obtained from Yahoo! Finance and are freely available at <https://finance.yahoo.com>. Market capitalisation corresponds to the last day in each data set. Each stock is represented by a time series, measuring the adjusted (for dividends, stock splits, and new stock offerings) daily closing price. Note that the initial date of each data set is conditioned by the first day in which all the companies composing it were quoted, hence the great variability in the number of available points.

### C. Forex' data

Forex stands for foreign exchange market, and is a global decentralised or over-the-counter market for the trading of currencies. It has some unique characteristics, including its large trading volume, its geographical dispersion, and its continuous operation (24 hours a day except for weekends). In this study we have considered two sets of 30 main currency pairs, reported in Tab. X. Data for each pair have been obtained from [HistData.com](https://www.histdata.com), and represent time series of prices with a 1 minute time resolution. In all cases, analysed data correspond to the period January 1st 2011 to December 31st 2023.

TABLE I. List of the 30 considered stocks part of the **S&P 500** index, sorted by alphabetic order; for each stock, the corresponding code and full names are reported.

AAPL	Apple Inc	ABBV	AbbVie Inc	ADBE	Adobe Inc
AMD	AMD	AMZN	Amazon.com Inc	AVGO	Broadcom Inc
BRK-B	Berkshire Hathaway Inc Class B	COST	Costco Wholesale Corporation	CRM	Salesforce Inc
CVX	Chevron Corp	GOOG	Alphabet Inc Class C	GOOGL	Alphabet Inc Class A
HD	Home Depot Inc	JNJ	Johnson & Johnson	JPM	JPMorgan Chase & Co
KO	Coca-Cola Co	LLY	Eli Lilly And Co	MA	Mastercard Inc
META	Meta Platforms Inc	MRK	Merck & Co Inc	MSFT	Microsoft Corp
NFLX	Netflix Inc	NVDA	NVIDIA Corp	PEP	PepsiCo Inc
PG	Procter & Gamble Co	TSLA	Tesla Inc	UNH	UnitedHealth Group Inc
V	Visa Inc	WMT	Walmart Inc	XOM	Exxon Mobil Corp

TABLE II. List of the 30 considered stocks part of the **DAX** index, sorted by alphabetic order; for each stock, the corresponding code and full names are reported.

ICOV.DE	Covestro AG	AIR.DE	Airbus SE
ADS.DE	Adidas AG	ALV.DE	Allianz SE
BAS.DE	BASF SE	BAYN.DE	Bayer AG
BEI.DE	Beiersdorf AG	BMW.DE	Bayerische Motoren Werke AG
CON.DE	Continental AG	DB1.DE	Deutsche Börse AG
DBK.DE	Deutsche Bank AG	DHL.DE	Deutsche Post AG
DTE.DE	Deutsche Telekom AG	DTG.DE	Daimler Truck Holding AG
ENR.DE	Siemens Energy AG	EOAN.DE	E.ON SE
FRE.DE	Fresenius SE	HEI.DE	Heidelberg Materials AG
HNR1.DE	Hannover Rück SE	IFX.DE	Infineon Technologies AG
MRK.DE	Merck KGaA	MTX.DE	MTU Aero Engines AG
P911.DE	Dr Ing hc F Porsche AG	RWE.DE	RWE AG
SHL.DE	Siemens Healthineers AG	SIE.DE	Siemens AG
SY1.DE	Symrise AG	VNA.DE	Vonovia SE
VOW3.DE	Volkswagen AG	ZAL.DE	Zalando SE

TABLE III. List of the 30 considered stocks part of the **Aggressive small caps** index, sorted by alphabetic order; for each stock, the corresponding code and full names are reported.

DHT	DHT Holdings Inc	ADUS	Addus Homecare Corporation
AGIO	Agios Pharmaceuticals Inc	AMBA	Ambarella Inc
BRP	BRP Group Inc	CAKE	Cheesecake Factory Inc
CEPU	Central Puerto ADR	CRTO	Criteo SA
EPAC	Enerpac Tool Group Corp	GNL	Global Net Lease Inc
GSBD	Goldman Sachs BDC Inc	HEES	H&E Equipment Services, Inc.
JBLU	JetBlue Airways Corporation	JELD	Jeld-Wen Holding Inc
LPG	Dorian LPG Ltd	MRCY	Mercury Systems Inc
MYGN	Myriad Genetics, Inc.	NGL-PB	NGL Energy Partners LP
NGL-PC	NGL Energy Partners LP	PARR	Par Pacific Holdings Inc
PEB	Pebblebrook Hotel Trust	PLMR	Palomar Holdings Inc
SAH	Sonic Automotive Inc	TBBK	Bancorp Inc
TDS	Telephone and Data Systems Inc	TNK	Teekay Tankers Ltd
TRMK	Trustmark Corp	UPST	Upstart Holdings Inc
USLM	United States Lime & Minerals Inc	YY	JOYY Inc

#### D. Weather (wind) data

Weather information has been extracted from METARs (METeorological Aerodrome Reports), i.e. reports describing the meteorological conditions at the largest European airports. These have been collected in real-time from the website [allmetsat.com](http://allmetsat.com) using an in-house software scraper with a time resolution of 30 minutes; and are composed of a text following the standard defined by the World Meteorological Organisation (WMO) [20].

Data were available from approximately April 25<sup>th</sup> 2019, to April 1<sup>st</sup> 2022, for a total of more than 51,000 reports.



TABLE IV. List of the 30 considered stocks part of the **FTSE 100** index, sorted by alphabetic order; for each stock, the corresponding code and full names are reported.

CCH.L	Coca-Cola HBC AG	AAF.L	Airtel Africa plc
AHT.L	Ashtead Group plc	ANTO.L	Antofagasta plc
AUTO.L	Auto Trader Group plc	BA.L	BAE Systems plc
BATS.L	British American Tobacco plc	CNA.L	Centrica plc
CPG.L	Compass Group plc	DPLM.L	Diploma plc
ENT.L	Entain plc	EXPN.L	Experian plc
EZJ.L	easyJet plc	HLN.L	Haleon plc
ICG.L	Intermediate Capital Group plc	MNG.L	M&G plc
PRU.L	Prudential plc	PSN.L	Persimmon plc
RMV.L	Rightmove plc	RR.L	Rolls-Royce Holdings plc
RTO.L	Rentokil Initial plc	SDR.L	Schroders plc
SHEL.L	Shell plc	SMIN.L	Smiths Group plc
SMT.L	Scottish Mortgage Investment Trust plc	SPX.L	Spirax-Sarco Engineering plc
SSE.L	SSE plc	STJ.L	St. James's Place plc
TSCO.L	Tesco plc	VOD.L	Vodafone Group plc

TABLE V. List of the 30 considered stocks part of the **Euro Stoxx 50** index, sorted by alphabetic order; for each stock, the corresponding code and full names are reported.

ABL.BR	Anheuser-Busch SA/NV	InBev	AI.PA	L'Air Liquide S.A.	AIR.PA	Airbus SE
ALV.DE	Allianz SE		ASML.AS	ASML Holding N.V.	BAS.DE	BASF SE
BAYN.DE	Bayer Aktiengesellschaft		BBVA.MC	Banco Bilbao Vizcaya Argentaria, S.A.	BMW.DE	Bayerische Motoren Werke Aktiengesellschaft
BN.PA	Danone S.A.		BNP.PA	BNP Paribas SA	CA.PA	Carrefour SA
CS.PA	AXA SA		DB1.DE	Deutsche Börse AG	DBK.DE	Deutsche Bank Aktiengesellschaft
DG.PA	Vinci SA		DHL.DE	Deutsche Post AG	DTE.DE	Deutsche Telekom AG
EL.PA	EssilorLuxottica SA		ENEL.MI	Enel SpA	ENGI.PA	Engie SA
ENI.MI	Eni S.p.A.		EOAN.DE	E.ON SE	FRE.DE	Fresenius SE & Co. KGaA
G.MI	Assicurazioni Generali S.p.A.		GLE.PA	Société Générale SA	BE.MC	Iberdrola, S.A.
INGA.AS	ING Groep N.V.		ISP.MI	Intesa Sanpaolo S.p.A.	RI.PA	Pernod Ricard SA

TABLE VI. List of the 30 considered stocks part of the **Down Jones Industrial Average (DJI)** index, sorted by alphabetic order; for each stock, the corresponding code and full names are reported.

AAPL	Apple Inc.	AMGN	Amgen Inc.	AXP	American Express Company
BA	The Boeing Company	CAT	Caterpillar Inc.	CRM	Salesforce, Inc.
CSCO	Cisco Systems, Inc.	CVX	Chevron Corporation	DIS	The Walt Disney Company
DOW	Dow Inc.	GS	The Goldman Sachs Group, Inc.	HD	The Home Depot, Inc.
HON	Honeywell International Inc.	IBM	International Business Machines Corporation	INTC	Intel Corporation
JNJ	Johnson & Johnson	JPM	JPMorgan Chase & Co.	KO	The Coca-Cola Company
MCD	McDonald's Corporation	MMM	3M Company	MRK	Merck & Co., Inc.
MSFT	Microsoft Corporation	NKE	NIKE, Inc.	PG	The Procter & Gamble Company
TRV	The Travelers Companies, Inc.	UNH	UnitedHealth Group Incorporated	V	Visa Inc.
VZ	Verizon Communications Inc.	WBA	Walgreens Boots Alliance, Inc.	WMT	Walmart Inc.

A custom-made parser has been developed to extract and store basic information from each report, including: the 4-letters ICAO code of the issuing airport, the date and time of validity, temperature and dew point, and wind speed. Only the latter meteorological variable has been used in this study.

Additionally, two sets of airports have been considered: the 30 largest ones in Europe (see Tab. XI), plus a larger

TABLE VII. List of the 30 considered stocks part of the **Hang Seng Index (HSI)** index, sorted by alphabetic order; for each stock, the corresponding code and full names are reported.

0002.HK	CLP Holdings Limited	0003.HK	The Hong Kong and China Gas Company Limited
0012.HK	Henderson Land Development Company Limited	0017.HK	New World Development Company Limited
0027.HK	Galaxy Entertainment Group Limited	0101.HK	Hang Lung Properties Limited
0241.HK	Alibaba Health Information Technology Limited	0267.HK	CITIC Limited
0669.HK	Techtronic Industries Company Limited	0883.HK	CNOOC Limited
0992.HK	Lenovo Group Limited	1038.HK	CK Infrastructure Holdings Limited
1044.HK	Hengan International Group Company Limited	1093.HK	CSPC Pharmaceutical Group Limited
1109.HK	China Resources Land Limited	1209.HK	China Resources Mixc Lifestyle Services Limited
1398.HK	Industrial and Commercial Bank of China Limited	1810.HK	Xiaomi Corporation
2020.HK	ANTA Sports Products Limited	2269.HK	WuXi Biologics (Cayman) Inc.
2319.HK	China Mengniu Dairy Company Limited	2331.HK	Li Ning Company Limited
2628.HK	China Life Insurance Company Limited	2688.HK	ENN Energy Holdings Limited
3690.HK	Meituan	6098.HK	Country Garden Services Holdings Company Limited
6690.HK	Haier Smart Home Co., Ltd.	9618.HK	JD.com, Inc.
9633.HK	Nongfu Spring Co., Ltd.	9988.HK	Alibaba Group Holding Limited

TABLE VIII. List of the 30 considered stocks part of the **FTSE Bursa Malaysia (KLSE)** index, sorted by alphabetic order; for each stock, the corresponding code and full names are reported.

1015.KL	AMMB Holdings Berhad	1023.KL	CIMB Group Holdings Berhad
1066.KL	RHB Bank Berhad	1082.KL	Hong Leong Financial Group Berhad
1155.KL	Malayan Banking Berhad	1295.KL	Public Bank Berhad
1961.KL	IOI Corporation Berhad	2445.KL	Kuala Lumpur Kepong Berhad
3182.KL	Genting Berhad	3816.KL	MISC Berhad
4065.KL	PPB Group Berhad	4197.KL	Sime Darby Berhad
4677.KL	YTL Corporation Berhad	4707.KL	Nestlé (Malaysia) Berhad
4715.KL	Genting Malaysia Berhad	4863.KL	Telekom Malaysia Berhad
5183.KL	PETRONAS Chemicals Group Berhad	5225.KL	IHH Healthcare Berhad
5285.KL	SD Guthrie Berhad	5296.KL	Mr D.I.Y. Group (M) Berhad
5347.KL	Tenaga Nasional Berhad	5681.KL	PETRONAS Dagangan Berhad
5819.KL	Hong Leong Bank Berhad	6012.KL	Maxis Berhad
6033.KL	PETRONAS Gas Berhad	6742.KL	YTL Power International Berhad
6888.KL	Axiata Group Berhad	6947.KL	Celcomdigi Berhad
7084.KL	QL Resources Berhad	8869.KL	Press Metal Aluminium Holdings Berhad

TABLE IX. List of the 30 considered stocks part of the **Straits Times Index (STI)** index, sorted by alphabetic order; for each stock, the corresponding code and full names are reported.

9CL.SI	CapitaLand Investment Limited	AJBU.SI	Keppel DC REIT
BN4.SI	Keppel Ltd.	BS6.SI	Yangzijiang Shipbuilding (Holdings) Ltd.
BUOU.SI	Frasers Logistics & Commercial Trust	C07.SI	Jardine Cycle & Carriage Limited
C09.SI	City Developments Limited	C38U.SI	CapitaLand Integrated Commercial Trust
C52.SI	ComfortDelGro Corporation Limited	D01.SI	DFI Retail Group Holdings Limited
D05.SI	DBS Group Holdings Ltd	EMI.SI	Emperador Inc.
F34.SI	Wilmar International Limited	G13.SI	Genting Singapore Limited
H78.SI	Hongkong Land Holdings Limited	J36.SI	Jardine Matheson Holdings Limited
J69U.SI	Frasers Centrepoint Trust	M44U.SI	Mapletree Logistics Trust
ME8U.SI	Mapletree Industrial Trust	N2IU.SI	Mapletree Pan Asia Commercial Trust
O39.SI	Oversea-Chinese Banking Corporation Limited	S51.SI	Seatrium Limited
S58.SI	SATS Ltd.	S63.SI	Singapore Technologies Engineering Ltd
U14.SI	UOL Group Limited	U96.SI	Sembcorp Industries Ltd
V03.SI	Venture Corporation Limited	Y92.SI	Thai Beverage Public Company Limited
YF8.SI	Yangzijiang Financial Holding Ltd.	Z74.SI	Singapore Telecommunications Limited

set of smaller airports (see Tab. XII) that are used to create extended networks.

TABLE X. List of the 30+30 considered currency pairs of the **Forex** market, sorted by alphabetic order. Names corresponding to each code are reported in the bottom part.

AUD-CAD	AUD-CHF	AUD-JPY	AUD-USD	AUX-AUD	CAD-JPY
CHF-JPY	EUR-AUD	EUR-CAD	EUR-CHF	EUR-GBP	EUR-JPY
EUR-NZD	EUR-USD	GBP-CHF	GBP-JPY	GBP-USD	GRX-EUR
NZD-CAD	NZD-JPY	NZD-USD	SGD-JPY	USD-CAD	USD-CHF
USD-HKD	USD-JPY	USD-MXN	USD-NOK	USD-TRY	XAU-USD

AUD-NZD	BCO-USD	CAD-CHF	EUR-CZK	EUR-DKK	EUR-HUF
EUR-NOK	EUR-PLN	EUR-SEK	EUR-TRY	FRX-EUR	GBP-AUD
GBP-CAD	GBP-NZD	HKX-HKD	JPX-JPY	NSX-USD	NZD-CHF
SPX-USD	UDX-USD	UKX-GBP	USD-CZK	USD-DKK	USD-HUF
USD-PLN	USD-SEK	USD-SGD	USD-ZAR	WTI-USD	ZAR-JPY

AUD: Australian Dollar	AUX: ASX 200	BCO: Brent crude oil
FRX: CAC 40	CAD: Canadian Dollar	CZK: Czech Koruna
DKK: Danish Krone	GRX: DAX 30	EUR: Euro
XAU: Gold	HKX: Han Seng	HKD: Hong Kong Dollar
HUF: Hungarian Forint	JPY: Japanese Yen	MXN: Mexican Peso
NZD: New Zealand Dollar	NOK: Norwegian Krone	PLN: Polish zloty
GBP: Pound sterling	SGD: Singapore Dollar	ZAR: South African Rand
SEK: Swedish Krona	CHF: Swiss Franc	TRY: Turkish lira
USD: United States Dollar	WTI: West Texas Intermediate	

TABLE XI. List of the 30 largest EU airports for which meteorological data have been extracted, including both their 4-letters ICAO code (i.e. their unique identifier in the original data set) and the full official name.

EGLL: Heathrow Airport	LFPG: Charles de Gaulle Airport
EHAM: Amsterdam Airport Schiphol	EDDF: Frankfurt am Main Airport
LEMD: Adolfo Suárez Madrid-Barajas Airport	LEBL: Josep Tarradellas Barcelona-El Prat Airport
EDDM: Munich Airport	EGKK: Gatwick Airport
LIRF: Leonardo da Vinci-Fiumicino Airport	LFPO: Orly Airport
EIDW: Dublin Airport	LSZH: Zurich Airport
EKCH: Copenhagen Airport	LEPA: Palma de Mallorca Airport
ENGM: Oslo Airport, Gardermoen	EGCC: Manchester Airport
EGSS: London Stansted Airport	LOWW: Vienna International Airport
ESSA: Stockholm Arlanda Airport	EBBR: Brussels Airport
LIMC: Malpensa Airport	EDDL: Düsseldorf Airport
LEMG: Málaga Airport	EPWA: Warsaw Chopin Airport
LSGG: Geneva Airport	EDDH: Hamburg Airport
LKPR: Václav Havel Airport Prague	EGGW: Luton Airport
LHBP: Budapest Ferenc Liszt International Airport	EGPH: Edinburgh Airport

### E. Air transport delay data

Time series representing the evolution of delays in the US air transport system have been reconstructed using data obtained from the Reporting Carrier On-Time Performance database of the Bureau of Transportation Statistics, U.S. Department of Transportation, freely accessible at <https://www.transtats.bts.gov>. This database contains information about flights operating in US airports, including departure and arrival time (both scheduled and executed), and consequently the associated delays. Data here considered cover years 2015 to 2019 (both included); note that more recent data, while available, have been disregarded, due to the abnormal dynamics experienced during the COVID-19 pandemics. From this data set, the arrival delay of each flight has been estimated, as the difference between the corresponding actual and scheduled landing times. Afterwards, a time series of hourly average delay has been calculated for each of the top-30 airports in terms of number of flights - see Tab. XIII.

TABLE XII. List of the additional EU airports used to reconstruct extended wind networks. As in Tab. XI, it includes the 4-letters ICAO code (i.e. their unique identifier in the original data set) and the full official name.

EBAW: Antwerp International Airport	EBCI: Brussels South Charleroi Airport
EBLG: Liege Airport	EBOS: Ostend-Bruges International Airport
EDDB: Berlin Brandenburg Airport	EDDC: Dresden Airport
EDDG: Münster Osnabrück Airport	EDDK: Cologne Bonn Airport
EDDN: Nuremberg Airport	EDDP: Leipzig/Halle Airport
EDDS: Stuttgart Airport	EDDV: Hannover Airport
EDDW: Bremen Airport	EDSB: Karlsruhe/Baden-Baden Airport
EETN: Lennart Meri Tallinn Airport	EFHK: Helsinki-Vantaa Airport
EFOU: Oulu Airport	EFRO: Rovaniemi Airport
EFTP: Tampere-Pirkkala Airport	EFTU: Turku Airport
EFVA: Vaasa Airport	EGBB: Birmingham Airport
EGJJ: Jersey Airport	EGNX: East Midlands Airport
EGPD: Aberdeen International Airport	EGPF: Glasgow Airport
EHBK: Maastricht Aachen Airport	EHRD: Rotterdam The Hague Airport
EINN: Shannon Airport	EKAH: Aarhus Airport
EKBI: Billund Airport	EKYT: Aalborg Airport
EPGD: Gdańsk Lech Wałęsa Airport	EPKK: Kraków John Paul II International Airport
EPKT: Katowice Wojciech Korfanty Airport	EPPO: Poznań-Ławica Henryk Wieniawski Airport
EPWR: Wrocław Airport	ESGG: Göteborg Landvetter Airport
ESMS: Malmö Airport	EVRA: RIX Riga Airport
EYKA: Kaunas Airport	EYVI: Vilnius International Airport
LATI: Tirana International Airport Nënë Tereza	LBBG: Burgas Airport
LBSF: Sofia Airport	LBWN: Varna Airport
LCLK: Larnaca International Airport	LCPH: Paphos International Airport
LDDU: Dubrovnik Ruder Bošković Airport	LDPL: Pula Airport
LDSP: Split Saint Jerome Airport	LDZA: Zagreb Franjo Tudman Airport
LDZD: Zadar Airport	LEAL: Alicante-Elche Miguel Hernández Airport
LEBB: Bilbao Airport	LEGE: Girona-Costa Brava Airport
LEIB: Ibiza Airport	LEJR: Jerez Airport
LEST: Santiago-Rosalía de Castro Airport	LEXJ: Santander Airport
LEZG: Zaragoza Airport	LEZL: Seville Airport
LFBD: Bordeaux-Mérignac Airport	LFBO: Toulouse-Blagnac Airport
LFBZ: Biarritz Pays Basque Airport	LFLL: Lyon-Saint-Exupéry Airport
LFML: Marseille Provence Airport	LFMN: Nice Côte d'Azur Airport
LFOB: Beauvais-Tillé Airport	LFQQ: Lille Airport
LFRB: Brest Bretagne Airport	LFRS: Nantes Atlantique Airport
LFSB: EuroAirport Basel Mulhouse Freiburg	LGSA: Chania International Airport Daskalogiannis
LHDC: Debrecen International Airport	LICC: Catania-Fontanarossa Airport
LIME: Orio al Serio International Airport	LIRP: Pisa International Airport
LJLJ: Ljubljana Jože Pučnik Airport	LKTB: Brno-Tuřany Airport
LMML: Malta International Airport	LOWG: Graz Airport
LOWI: Innsbruck Airport	LOWK: Klagenfurt Airport
LOWL: Linz Airport	LOWS: Salzburg Airport
LPMA: Madeira Airport	LPPR: Porto Airport
LRCL: Avram Iancu Cluj International Airport	LRIA: Iași International Airport
LROP: Henri Coanda International Airport	LRTR: Timișoara Traian Vuia International Airport
LSZA: Lugano Airport	LSZB: Bern-Belp Regional Aerodrome
LTAC: Ankara Esenboğa Airport	LTAF: Adana Şakirpaşa Airport
LTAI: Antalya Airport	LTBA: Atatürk Airport
LTBJ: İzmir Adnan Menderes Airport	LTBS: Dalaman Airport
LTCG: Trabzon Airport	LTFE: Milas-Bodrum Airport
LTfJ: Istanbul Sabiha Gökçen International Airport	LTfM: Istanbul Airport
LUKK: Chișinău International Airport	LWSK: Skopje International Airport
LYBE: Belgrade Nikola Tesla Airport	LZIB: Bratislava Airport

TABLE XIII. List of the 30 largest US airports composing the air transport delay data.

Hartsfield-Jackson Atlanta International Airport	Denver International Airport
Dallas Fort Worth International Airport	Los Angeles International Airport
Chicago O'Hare International Airport	Phoenix Sky Harbor International Airport
Minneapolis-Saint Paul International Airport	Charlotte Douglas International Airport
Seattle-Tacoma International Airport	San Francisco International Airport
John F. Kennedy International Airport	George Bush Intercontinental Airport
Orlando International Airport	Newark Liberty International Airport
Harry Reid International Airport	Fort Lauderdale-Hollywood International Airport
General Edward Lawrence Logan International Airport	Detroit Metropolitan Wayne County Airport
Miami International Airport	LaGuardia Airport
Washington Dulles International Airport	Baltimore/Washington International Thurgood Marshall Airport
Philadelphia International Airport	San Diego International Airport
Chicago Midway International Airport	Salt Lake City International Airport
Ronald Reagan Washington National Airport	Tampa International Airport
Portland International Airport	St. Louis Lambert International Airport

TABLE XIV. List of the 30 regions with the highest number of incoming visitors to Canada. The list include both the name of the region, as defined in the original data set, and the total number of visitors in the considered time window.

United Kingdom: 2.250.596	France: 2.214.186
Mexico: 1.499.043	Germany: 940.731
Americas countries other than the United States of America - other countries: 382.235	Netherlands: 367.473
Brazil: 352.235	Switzerland: 337.682
Italy: 278.597	Belgium: 217.295
Spain: 213.824	Ireland: 208.233
Europe - other countries: 203.574	Israel: 136.226
Jamaica: 114.370	Sweden: 110.847
Colombia: 94.151	Denmark: 93.236
Austria: 90.445	Portugal: 87.292
Chile: 82.686	Poland: 79.915
Trinidad and Tobago: 71.130	Norway: 65.322
Ukraine: 58.927	Turkey: 52.242
Bahamas: 50.832	Romania: 50.712
Czechia: 49.808	Bermuda: 46.380

## F. Canadian borders' data

This data set includes data about the number of daily foreign visitors entering Canada; it is collected by Statistics Canada, i.e. the national statistical office of Canada, and is freely available at <https://www150.statcan.gc.ca/t1/tb11/en/cv.action?pid=2410005601>. Data have been obtained from January 1<sup>st</sup> 2018 to December 31<sup>st</sup> 2023, and include the daily number of visitors, arriving in any transportation mode, from the 30 largest incoming countries and regions - a full list is reported in Tab. XIV.

## II. DATA PREPROCESSING

### A. EEG data

For the creation of each network of either a control subject or a PD patient, a random recording from the corresponding group has been selected, for then extracting a segment of length  $w$  starting from a random position. The output is then a set of 30 time series of length  $w$ , to which we applied an automatic artefact removal procedure based on subtracting the two main components as detected by an Independent Component Analysis. The resulting time series have further been analysed for the presence of silent sequences, suggesting that the data of the channel were not recorded correctly, and for values exceeding  $\pm 300$  microvolts; if any such instance was detected, the whole set was discarded, and the process was performed again.

It is worth noting that all results here presented correspond to the analysis of the broadband signal, as yielded by the EEG machine. For the sake of completeness, we further tested the effect of reconstructing functional networks (see Sec. III) on signals filtered according to four standard frequency bands, namely  $\alpha$  (8 - 13Hz),  $\beta_1$  (13 - 20Hz),  $\beta_2$  (20 - 30Hz), and  $\gamma$  (30 - 50Hz). In all cases, the processing has been performed with a fourth order Butterworth filter. The resulting networks present much smaller differences between control subjects and patients, as represented by the corresponding classification score in Fig. 1; the frequency band approach has then been discarded.

### B. Stock markets' data

To create the stock market's networks, we selected the adjusted close price daily time series for the companies composing the chosen market. These raw time series start on the day of the opening of the youngest company on the market. In the case of Euro Stoxx 50, holidays in different countries where companies remained closed were removed from the time series. Then, for every time series, a logarithmic normalisation is applied to obtain a representation of the relative increase or decrease in the adjusted closed price with respect to the previous day. As customary, this is done through the transformation:

$$\hat{x}(t) = \log_2 \frac{x(t)}{x(t-1)}. \quad (1)$$

The output is therefore 30 normalised time series for each market described in the previous section (Sec. I).

### C. Forex' data

Forex' time series were characterised by some missing data, which especially affected the beginning and the end of each year and major international holidays. These were dealt with by firstly associating a UNIX time stamp to

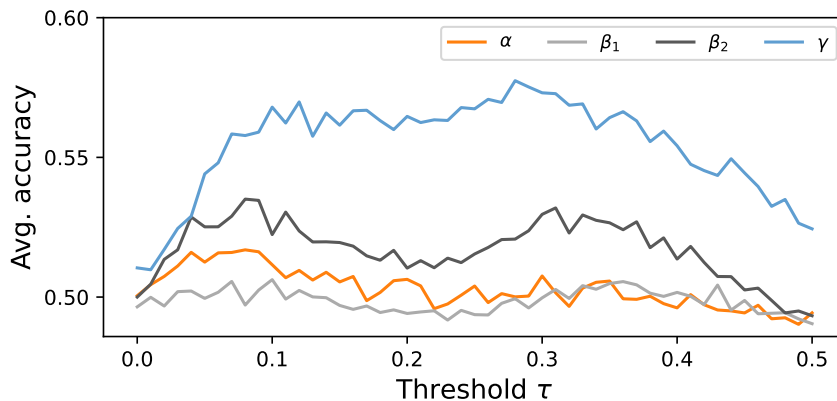


FIG. 1. Evolution of the classification score between functional networks of control subjects and patients, when the corresponding time series are filtered according to four standard frequency bands (see legend for colour codes). Results are reported as the average accuracy over 500 independent realisations, as a function of the threshold  $\tau$  - see Sec. III for details.

each available data point, i.e. a number representing the elapsed time in seconds since a reference moment; secondly, missing points were recovered using a piece-wise linear interpolation. As a final step, time series have been transformed according to the logarithm of the ratio between consecutive time points, see Eq. 1. No additional processing has been performed.

#### D. Weather (wind) data

The wind speed data obtained for each airport have firstly been converted to knots, in those few cases in which they were reported in other units (e.g. meters per second). Secondly, due to both internal technical limitations (e.g. connectivity losses) and to the incompleteness of the original data, a small fraction of time points were missing. Note that airports were initially filtered, and those for which more than 10% of the reports were missing, or for which more than five times data were missing in consecutive gaps of 6 or more hours, were already excluded. Hence, the few remaining instances of missing data have been solved by resorting to a linear interpolation.

#### E. Air transport delay data

Time series representing the dynamics of air transport are highly non-stationary, i.e. their evolution is a function of time; to illustrate, delays mostly appear whenever there is an increase in the number of operations, and are thus larger during the mid-day peak hours, for then substantially dropping in late hours of the day. Note that the presence of such regular trends may lead to an overestimation of the functional connectivity between airports. To solve this problem, each time series  $x(t)$  is transformed to the corresponding Z-Score, defined as:

$$z(t) = \frac{x(t) - \overline{x(t+24k)}}{\sigma_{x(t+24k)}}, \quad (2)$$

with  $k = (\dots, -2, -1, 1, 2, \dots)$ ,  $\bar{\cdot}$  being the average operator, and  $\sigma$  the standard deviation. In other words, each value  $z(t)$  represents the deviation of the observed metric from what expected at the same time in neighbouring days. Regularities appearing at specific time windows are therefore removed, and the resulting time series are highly stationary.

#### F. Canadian borders' data

The time series obtained from Statistics Canada have been transformed according to the logarithm of the ratio between consecutive days, i.e. following the same procedure for pre-processing financial data - see Eq. 1. No additional processing has been performed.

### III. NETWORK RECONSTRUCTION

For each complex system and each data set previously described in Sec. II, the available information includes a set of 30 time series, which are the starting point for the reconstruction of the corresponding functional networks. Given a window length  $w$  and a functional metric (i.e. linear correlation, rank correlation, Granger Causality or Transfer Entropy), the same random segment of length  $w$  is selected from the 30 time series, and the connectivity between all pairs of them is computed. For the sake of completeness, a short description of these functional metrics is here provided:

- Linear Correlation (LC). Pearson's linear correlation between the two considered time series.
- Rank Correlation (RC). Spearman's rank correlation between the two analysed time series.
- Granger Causality (GC). A classical example of a *predictive causality* test [21]. GC is based on assessing whether the inclusion of information about the dynamics of the causing element helps predict the future dynamics of the caused one [16]. The test is based on comparing two forecast models, usually constructed around autoregressive-moving-average (ARMA) models, respectively including or not information about the past of the causing element; for finally performing an F-test on the residuals, and thus obtaining a  $p$ -value assessing whether the causing element contributes with relevant information - and hence, whether a causality relationship is present.
- Transfer Entropy (TE). TE can be seen as a generalisation of GC based on information-theoretic concepts; and aims at quantifying the reduction in uncertainty of a future value of the caused dynamics due to the history of the cause. In other words, TE evaluates the extra information that the historical state of the cause provides about the next observation in the caused element. The concept of Transfer Entropy was pioneered independently by Schreiber [17] and Paluš [22], and is mathematically formalised as:

$$TE_{X \rightarrow Y(k,l)} = \sum_{x \in X, y \in Y} p(y_{n+1}, y_n^{(l)}, x_n^{(k)}) \log \left( \frac{p(y_{n+1} | y_n^{(l)}, x_n^{(k)})}{p(y_{n+1} | y_n^{(l)})} \right). \quad (3)$$

$l$  and  $k$  denote the embedding vectors, i.e. the past values of the  $Y$  and  $X$  processes, such that for instance  $x_n^{(k)}$  corresponds to  $(x_n, \dots, x_{n-k+1})$ . By capturing the direct exchange of information between two variables and being sensitive to non-linear attributes, TE is one of the most powerful measures for functional network reconstruction [18].

In the case of the LC and the RC, we account for the time delay in the information transmission between two time series by finding the maximum value obtained by shifting one of the time series relative to the other by up to 5 time points. Note that this process is inherently included in the GC and the TE, and is not needed.

The result of this analysis is a connectivity value for each pair of time series, which can be interpreted as the weighted adjacency matrix of a network, where nodes represent time series and edge weights the connectivity (either correlation or causality) between them. The result is thus a complete weighted network.

As a final step, these complete networks are pruned, by applying a threshold  $\tau$  to the edges. This is used to create two different networks:

- Unweighted networks: all links with a weight lower than  $\tau$  are deleted, and the weight of the surviving links is further deleted - thus creating a sparse unweighted network.
- Weighted networks: links whose weight is lower than  $\tau$  are deleted, but the weight of the remainder links is preserved; the result is therefore a sparse network with weighted links.



## IV. NETWORK OPTIMISATION

### A. General procedure

As previously described, the reconstruction of a functional network relies on two parameters: the segment length  $l$  and the threshold  $\tau$  - note that a third parameter, representing a temporal downsampling of the data, will be further studied in Sec. VII. We here discuss how the best combination of parameters has been obtained in each case; note that the same procedure has independently been applied to both weighted and unweighted networks.

#### *EEG brain networks*

The procedure starts by fixing  $l = 1,000$ , both for networks corresponding to control subjects and patients suffering from Parkinson's Disease; the threshold  $\tau$  is then varied between 0.0 and 0.5, in steps of 0.01. The best  $\tau$ , i.e. the one for which the classification score is maximal, is retained; and afterwards  $l$  is varied between 100 and 2,000, in steps of 100, again retaining the value yielding a maximal classification score.

The same procedure is independently applied to optimise the network reconstruction for the four functional metrics previously described; and for data filtered in specific frequency bands, as shown in Fig. 1.

#### *S&P 500, Forex, winds, air delays, Canadian borders*

The optimisation procedure is also a greedy one, similar to the previous case: the threshold  $\tau$  is initially fixed to 0.2, and the segment length  $l$  is varied (in this case, the range has been independently estimated for each data set, see the corresponding graphs); once the best  $l$  is obtained,  $\tau$  is varied between 0.0 and 0.5. The main difference is that, in this case, we consider that the parameter is optimal when it minimises the classification score between the considered networks and the EEG ones, as the objective is to find comparable representations.

#### *Additional stock markets*

In order to evaluate the generalisability of the parameters previously obtained, the following additional stock markets have been considered: DJI, Euro Stoxx 50, Aggressive Small Caps, DAX, FTSE, HSI, KLSE, and STI - see Sec. I for details. In the case of these data sets, the networks have been reconstructed using the same parameters as the ones obtained for the S&P 500 one; i.e., no further optimisation has been performed.

#### *Extended data sets*

In the case of Forex, NASDAQ 500k, and winds, more time series were available, beyond the 30 initially considered. In order to assess the generalisability of the procedure, 2,000 random sets of time series have been extracted from each data set, and the corresponding functional networks have been reconstructed using the same parameters as the initial case. Results are reported in Fig. 3 of the main manuscript.

## B. Optimisation of winds' networks

The optimisation and reconstruction of winds' networks have followed the same procedures as all other complex systems; the results have nevertheless been omitted from Fig. 1 in the main manuscript, and are here reported instead for the sake of clarity. Specifically, Fig. 2 below depicts the evolution of the classification score as a function of the segment length  $l$  and of the applied thresholds  $\tau$ . While results for weighted networks (see bottom panels) are comparable to what obtained for other complex systems, unweighted networks (top panels) present a minimum for very long time scales. In order to reduce the impact of the noise, we calculated a second-order polynomial fit of the curve between  $l = 600$  and 1300 (see black solid line in the left panel); and the optimal time series length has been defined as the minimum of that fit. The impact of the use of such long segments, and specifically the relationship of this with the system characteristic time scale, will be further discussed in Sec. VII below.

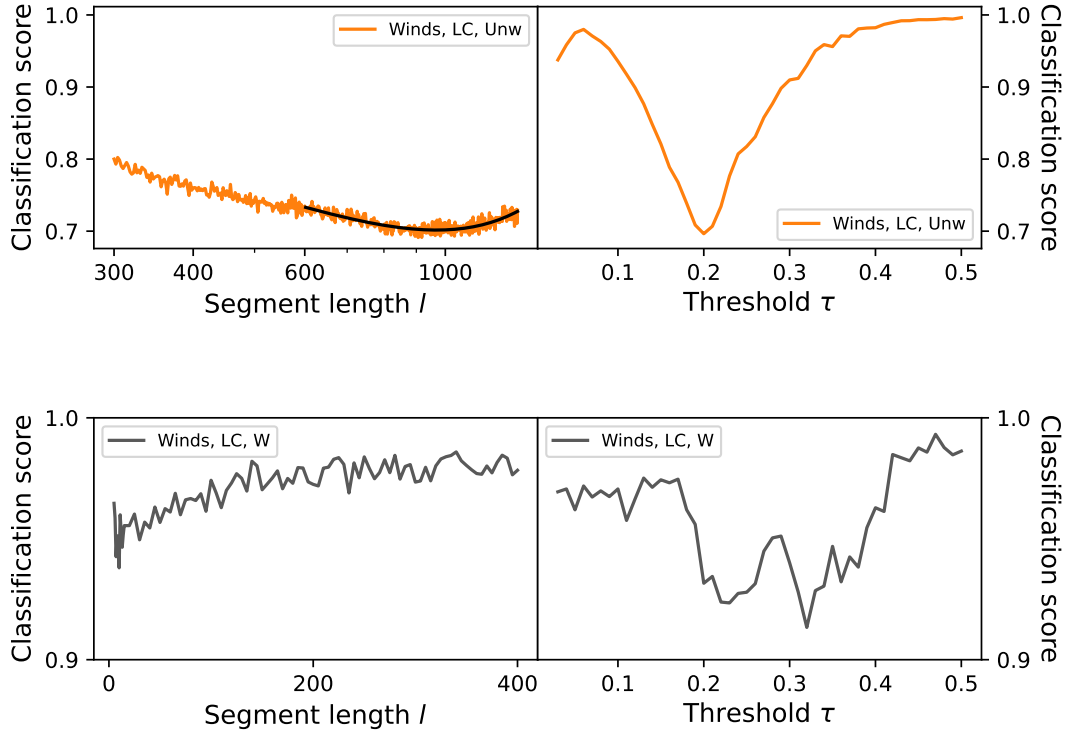


FIG. 2. Classification score between between functional brain networks of control subjects and those obtained from wind data, both unweighted (top panels) and weighted (bottom panels), as a function of the segment length  $l$  (left panels) and the threshold  $\tau$  (right panel). The black solid line in the top left panel reports the best fit of a second-order polynomial function, between  $l = 600$  and 1300.

### C. Optimality of the optimisation process

The attentive reader will have noted that the optimisation process here used is a greedy one, in which the impact of changing the two parameters is evaluated sequentially. In order to check that this is not biasing the results, Fig. 3 reports an analysis of the classification score, for Forex functional networks, around the optimal parameter set previously identified (i.e.  $l = 28$  and  $\tau = 0.3$ ). It can be appreciated that the solution obtained (with a classification score of 0.588) is very close to the global optimum (minimum score of 0.571); hence the use of a greedy optimisation does not significantly impact results, but allows to substantially reduce the computational cost of the analysis.

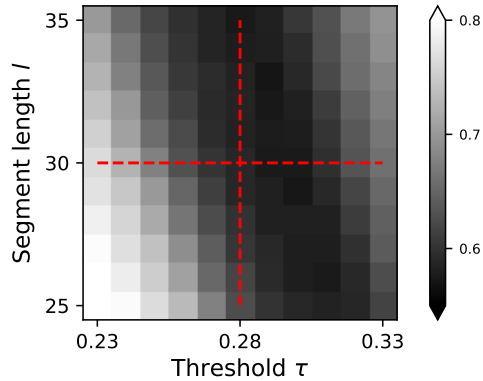


FIG. 3. Classification score of Forex networks as a function of the segment length  $l$  and the threshold  $\tau$ . Red lines indicate the solution found by the greedy optimisation, i.e.  $l = 28$  and  $\tau = 0.3$ .

### D. Synthesis of network reconstruction parameters

For the sake of clarity, we report in Tab. XV a synthesis of the optimal parameters used in the reconstruction of each functional network set, including values of  $l$ ,  $\tau$ , and the downsampling  $\gamma$  (further analysed in Sec. VII). The fifth column further reports the real time duration of the data segments used for each data set.

TABLE XV. Synthesis of the best parameters used in the reconstruction of each set of functional networks. The column real time indicates the time represented by  $l$  in the real evolution of the system. Rows in italic correspond to systems for which the parameters of another one have been used.

Data set	Filter	Length $l$	Threshold $\tau$	Real time	Downsampling $\gamma$
Brain	Unweighted	1400	0.2	2.8s	-
	Weighted	1400	0.29	2.8s	-
Forex	Unweighted	28	0.3	28 min	95
	Weighted	22	0.18	22 min	-
S&P500	Unweighted	33	0.21	33 days	-
	Weighted	31	0.2	31 days	-
<i>DJI</i>	<i>Unweighted</i>	<i>33</i>	<i>0.2</i>	<i>33 days</i>	-
<i>EuroStoxx 500</i>	<i>Unweighted</i>	<i>33</i>	<i>0.2</i>	<i>33 days</i>	-
<i>ASC</i>	<i>Unweighted</i>	<i>33</i>	<i>0.2</i>	<i>33 days</i>	-
<i>DAX</i>	<i>Unweighted</i>	<i>33</i>	<i>0.2</i>	<i>33 days</i>	-
<i>FTSE</i>	<i>Unweighted</i>	<i>33</i>	<i>0.2</i>	<i>33 days</i>	-
<i>HSI</i>	<i>Unweighted</i>	<i>33</i>	<i>0.2</i>	<i>33 days</i>	-
<i>KLSE</i>	<i>Unweighted</i>	<i>33</i>	<i>0.2</i>	<i>33 days</i>	-
<i>STI</i>	<i>Unweighted</i>	<i>33</i>	<i>0.2</i>	<i>33 days</i>	-
Winds	Unweighted	968	0.2	20 days	1
	Weighted	10	0.32	5 hours	-
Air delays	Unweighted	21	0.25	21 hours	-
	Weighted	10	0.19	10 hours	-
Canadian	Unweighted	32	0.26	32 days	-
	Weighted	7	0.31	7 days	-

## V. NETWORK ANALYSIS

### A. Financial networks and market volume

As a potential explanation of the differences in identifiability we observe across different stock markets, we here explore the relationship between this and their trading volume. Note that, according to the Efficient Market Hypothesis [23–25], larger (and more mature) markets should be more efficient, in the sense that information is more evenly distributed among participants, and this should result in clearer computations. Fig. 4 reports scatter plots of the average classification score as a function of the market capitalisation (left panel) and of the average trading volume (in number of stocks, right panel). No clear trend can be identified; size can thus be discarded as an explaining factor.

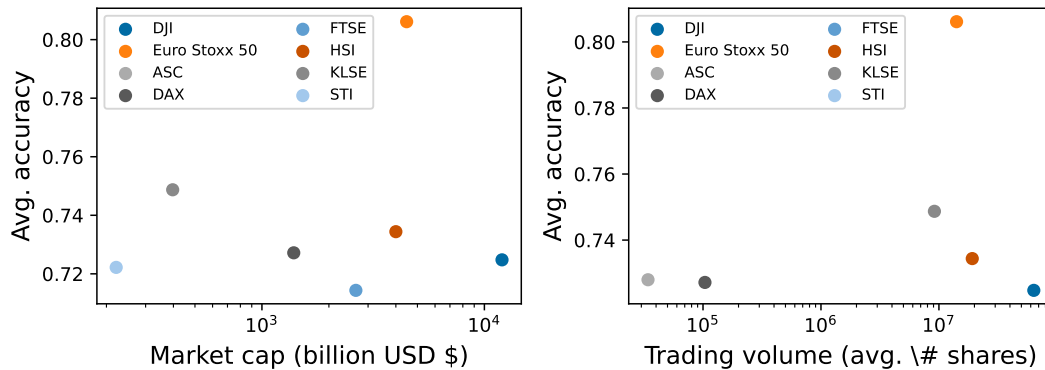


FIG. 4. Average classification score for eight considered stock markets, as a function of their market capitalisation (left panel) and the average daily trading volume (right panel).

## B. Winds' networks and spatial location

Following the previous case, we here analyse the relationship between the identifiability of winds' networks, and the geographical dispersion of the nodes (i.e. airports) composing them. Using the full list of available airports (see Tab. XII), 2,000 subsets of 30 random airports have been selected, for then evaluating their identifiability. The obtained classification score has then been compared to several properties of the distribution of distances between pairs of airports, as reported in Fig. 5 and Tab. XVI.

A linear fit between the score and each property always yields statistically significant results (see Tab. XVI), although a graphical representation of such fits hardly supports the presence of a relationship (see Fig. 5). These fits suggest that networks are less identifiable (i.e., more similar to EEG ones) when airports are close together, and are further homogeneously distributed.

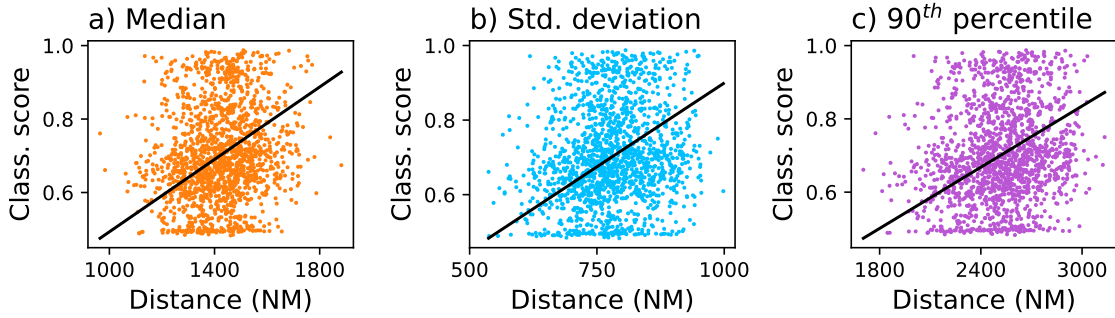


FIG. 5. Scatter plots of the classification score obtained for winds' networks, as a function of the median (left), standard deviation (centre), and 90<sup>th</sup> percentile (right) of the distance between the airports in there included. The black lines represent the best linear fit.

TABLE XVI. Details of the linear fits between the classification score obtained for winds' networks, and seven metrics extracted from the distribution of distances between pairs of airports in them included.

Statistics	Slope	Intercept	$R^2$	$p$ -value
Mean	0.000168	0.466	0.169	$< 8 \cdot 10^{-12}$
Median	0.000136	0.525	0.149	$< 10^{-9}$
Standard deviation	0.000266	0.497	0.161	$< 7 \cdot 10^{-11}$
Minimum	0.000310	0.685	0.064	$< 10^{-2}$
Maximum	0.000027	0.601	0.100	$< 5 \cdot 10^{-5}$
10 <sup>th</sup> percentile	0.000242	0.587	0.111	$< 8 \cdot 10^{-6}$
90 <sup>th</sup> percentile	0.000099	0.455	0.180	$< 5 \cdot 10^{-13}$

### C. Topological metrics

In order to understand whether the similarity observed between functional networks representing the brain activity of control subjects and the Forex ones is biased by the use of a DL model, we here compare the topological properties of both sets of networks. These are metrics that describe specific aspects of the structure of a network, and therefore allow to synthesise it in single values. For each network we calculated the following six standard metrics:

- *Assortativity*: metric measuring the tendency of the nodes of a network to be connected to nodes with degree (number of connections) very similar to it [26]. It is calculated as the Pearson’s correlation coefficient between the degree of nodes at both end of each link.
- *Transitivity*: tendency of the network to form triangles, i.e. triplets of nodes connected between them, normalised by the total number of possible triplets [27].
- *Efficiency*: calculated as the mean inverse distance between pairs of nodes of the network, it indicates how easily information can move between nodes [28].
- *Modularity*: tendency of the network of organising in communities, i.e. groups of nodes strongly connected between them but loosely connected with the remainder ones [29, 30]. The community structure is here estimated using the Louvain algorithm [31].
- *S Metric*: metric describing the presence of a “hub-like core”, where hubs (i.e. nodes with a large number of connections) are also connected between themselves to form a core [32]. It is defined as:

$$s = \sum_{i,j} d_i d_j, \quad (4)$$

with  $d_i$  being the degree (or number of links) of node  $i$ , and  $i$  and  $j$  representing the end nodes of all links in the network.

- *Network Information Content (NIC)*: measurement of the presence of regularities in the adjacency matrix, and hence of the amount of information encoded within the structure of the network [33]. It is calculated by merging pairs of nodes that imply the lowest loss of information, until shrinking the network into a single node.

All these metrics, with the exception of the modularity, depend on the number of nodes and of links in the network, and not only on the topological structure they aim at describing. To illustrate, the larger the number of links in the network, the easier is to obtain triangles by chance. In order to normalise these metrics, and thus allow comparisons between networks of different sizes, we resort to a null model composed of random equivalent (same number of nodes and links) networks. The original metric is then expressed through the corresponding Z-Score, which then represents how an observed metric deviates from randomness.

Each of the top six panels of Fig. 6 reports two histograms, comparing the probability distribution of the metric values for the unweighted functional networks of healthy control subjects (blue) and Forex (orange). No pair of distributions are exactly the same - a two-sample Kolmogorov-Smirnov test only accepts equality for the modularity for a significance level  $\alpha = 0.01$ . Still, most metrics are very similar in both cases, and the differences are not enough to classify individual networks.

In order to exclude that those differences could actually be used in a classification task, we have further trained a Random Forest (RF) model with such topological features and evaluated its performance. The RF is a classical Machine Learning model widely used in classification tasks, which provides both good accuracy and low tendency to overfitting - see Ref. [34] for an in-depth description. Results here correspond to a set of 500 tasks; in each one of them, a random half of the data was used for training, and the remainder for testing. The final score has then been assessed through the corresponding accuracy, as in the case of the DL classification. The bottom panel of Fig. 6 indicates that the RF model trained over topological features is in general better than the DL one, and is further more stable - note how the latter at times does not converge to a solution, hence the bimodal distribution. Still, the median score obtained by the RF model (68.6%) is not much higher than the DL’s one, and still supports the main arguments of this work.

We performed the same analyses on the functional networks of control subjects and PD patients, in order to recover the main classification task presented in the manuscript. As can be seen in Fig. 7, differences in topological metrics are minimal, and this results in a limited capacity of the RF model to discriminate between the two groups.

In short, results obtained by the DL model are qualitatively similar to those that could be obtained by standard Machine Learning models trained on the topological properties of the networks. The reasons behind the difference between them, and specifically why the RF model outperforms DL in Fig. 6, are open questions at the moment.

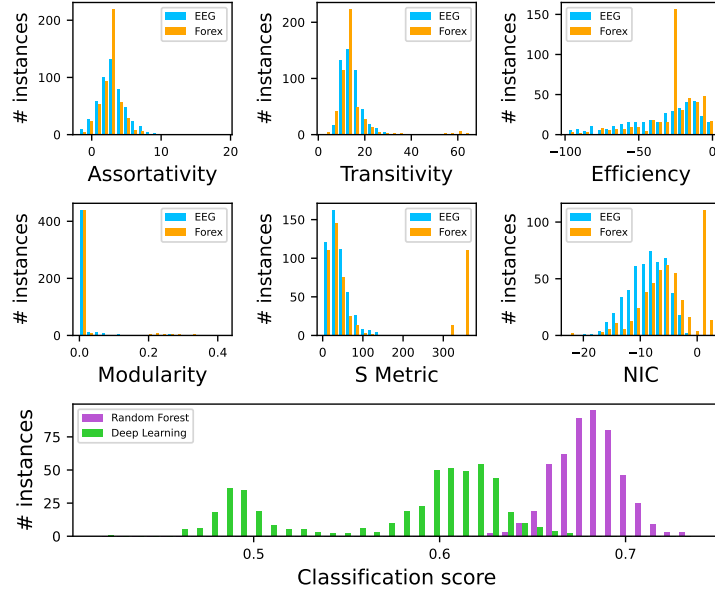


FIG. 6. Comparing functional networks of control subjects and Forex. The top six panels report histograms of the values of topological metrics of these networks, for EEG (blue bars) and Forex (orange bars) networks; see text for metric definitions. The bottom panel reports the distributions of the classification score obtained by Random Forest (magenta bars) and Deep Learning (green bars) models, the former being trained on the aforementioned topological metrics.

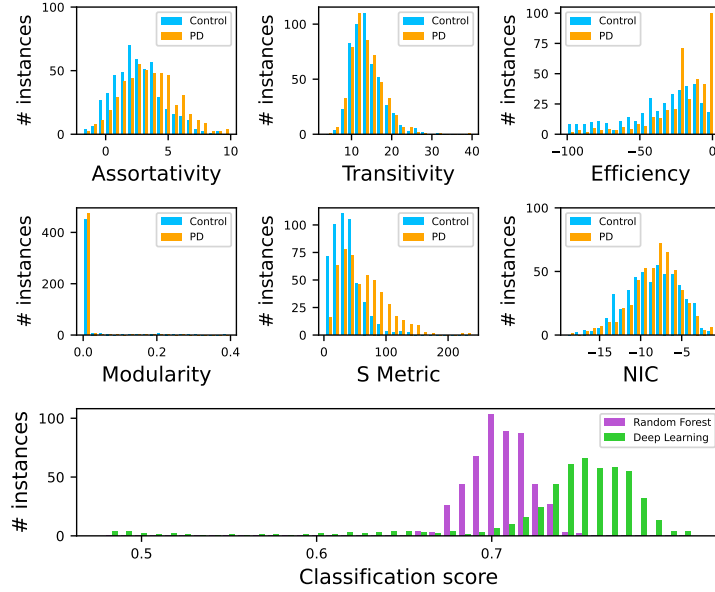


FIG. 7. Comparing functional networks of control subjects and Parkinson's patients. The top six panels report histograms of the values of topological metrics of these networks, for control subjects' (blue bars) and PD patients' (orange bars) networks; see text for metric definitions. The bottom panel reports the distributions of the classification score obtained by Random Forest (magenta bars) and Deep Learning (green bars) models, the former being trained on the aforementioned topological metrics.

### D. Motifs

Motifs, i.e. patterns of connectivity involved a limited number of nodes that appear with a frequency higher than what expected at random, have frequency been associated with computation of information in networks. We therefore tried to understand whether the appearance of motifs is somehow related with the similarity with EEG networks.

Towards this aim, Fig. 8 reports the Z-Score of 3- and 4-nodes undirected motifs as a function of the observed classification score. The Z-Score has been calculated as the number of standard deviations the observed number of instances deviates from what expected in ensembles of  $10^3$  random equivalent (i.e. same number of nodes and links) networks. We further report results for the EEG functional networks of control subjects; the top-30 Forex networks; the same Forex networks, when time series have been downsampled 1 : 100; and winds, air delays, and Canadian borders networks - see top legend in Fig. 8.

The motifs showing the higher appearance frequency are the fully connected triplets and quadruplets of nodes; on the other hand, large negative Z-Scores are associated with incomplete triplets (i.e. lines) and quadruplets (i.e. rings). These results are in line with that presented in the previous section, and especially the high values observed for the S metric (see Figs. 6 and 7); and suggest the presence of core groups of nodes strongly connected between themselves, creating a core-periphery configuration. Still, the presence of such structure is not enough to justify the similarity between networks, as illustrated by the similar motif values obtained in the case of air delays and Canadian border networks.

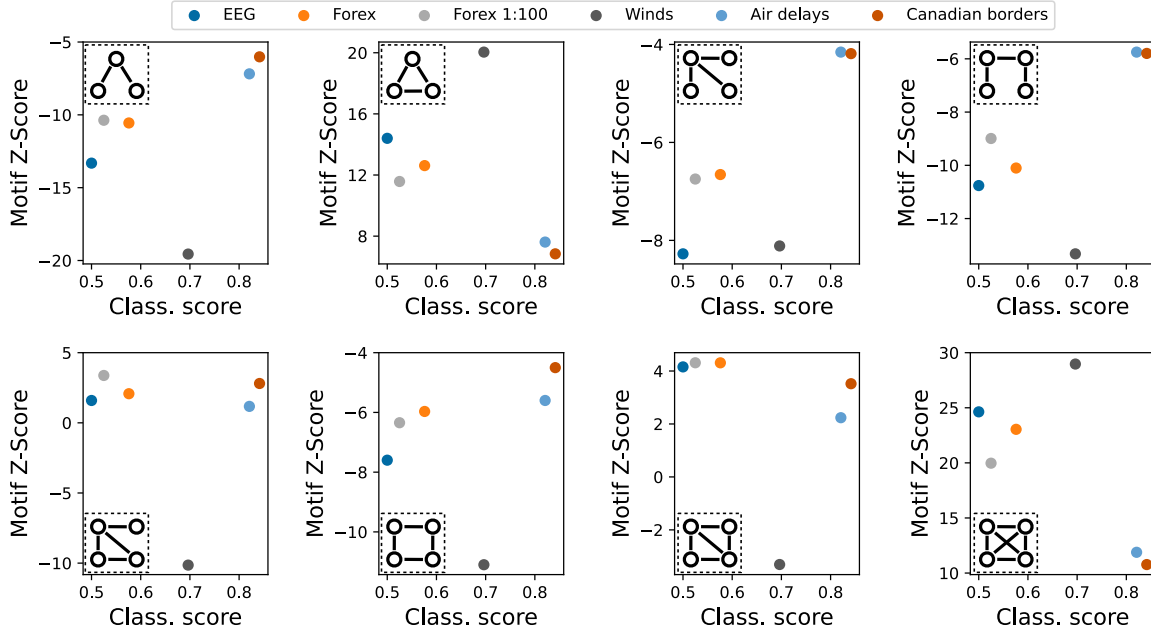


FIG. 8. Scatter plot of the Z-Score of 3- and 4-nodes motifs as a function of the classification score, as observed in sets of 1000 networks representing the complex systems reported in the legend. Networks have been reconstructed according to the optimal classification score.



## VI. SENSITIVITY ANALYSIS

With the aim to assess whether low classification scores are really significant, and not just a lack of sensitivity of the DL model, we analyse how these scores are affected by controlled changes in the network topology. We specifically consider the set of unweighted functional networks obtained for healthy control subjects, and a second set of these with some properties being modified; for finally performing a classification between them.

The first scenario consists of a random rewiring, in which two pairs of nodes  $n_{1...4}$  are randomly selected, such that a link between  $n_1$  and  $n_2$  exists, but  $n_3$  and  $n_4$  are disconnected. We then proceed to move the link from  $n_1 - n_2$  to  $n_3 - n_4$ , thus achieving a slightly modified topology. The left panel of Fig. 9 reports the evolution of the median classification score as a function of the fraction of links modified.

As a second scenario, we add a normally distributed noise to the original time series before reconstructing the functional networks - effectively driving the topology towards a random structure. The right panel of Fig. 9 reports the evolution of the classification score as a function of the standard deviation  $\sigma$  of such noise, normalised against the standard deviation of the corresponding EEG time series. As a reference, the dashed grey line (right Y scale) depicts the corresponding fraction of links that have changed, with respect to the networks reconstructed without noise.

A transition can be observed in both cases, with the score substantially increasing when more than 5% of the links are perturbed. It can therefore be concluded that the DL model is quite sensitive to changes in the structure, as very similar networks are needed to obtain low classification scores.

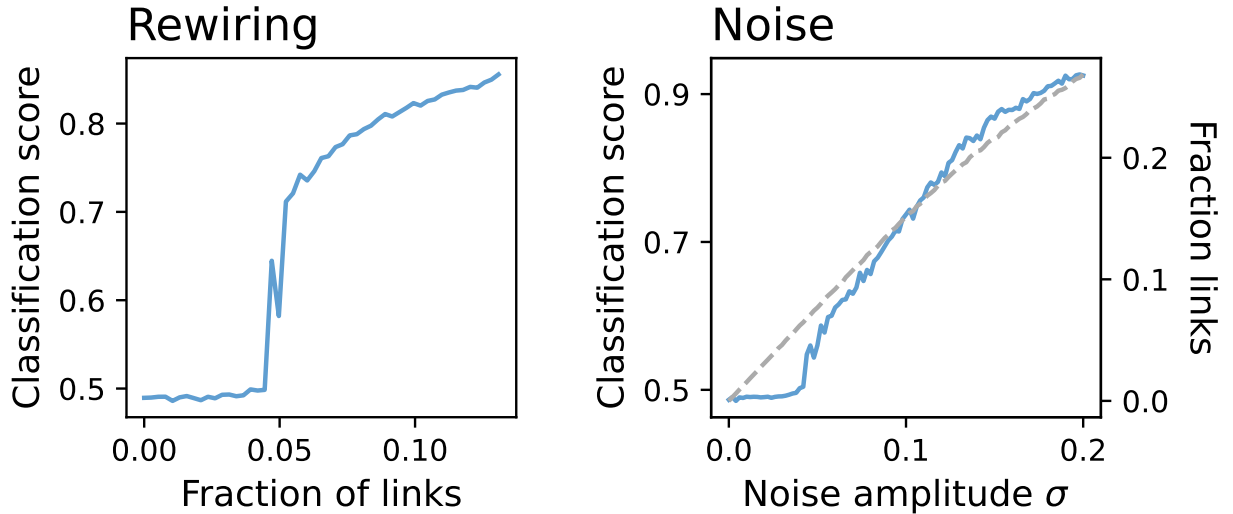


FIG. 9. Evolution of the classification score when comparing unweighted networks with slightly altered topology, as a function of the fraction of links randomly rewired (top panel), and of the amplitude of a uniformly distributed observational noise (bottom panel). In the latter case, the dashed grey line (right Y axis) reports the evolution of the fraction of altered links.

## VII. TEMPORAL DOWNSAMPLING

Any dynamical system is expected to have one or multiple characteristic time scales, on which the evolution mainly takes place. While these have been extensively studied in the human brain [35–38], fewer is known for other complex systems, and especially the ones here considered. Consequently, we here consider a downsampling of the original time series, for the Forex and Winds systems - i.e. the two with the higher timer resolution. In both cases, one every  $\gamma$  points in the original data have been preserved, while discarding all others. Besides this, the reconstruction has been performed using the best parameters (i.e. time segment lengths and thresholds) previously obtained in each case.

The evolution of the classification score as a function of the downsampling factor  $\gamma$  is presented in Fig. 10. The classification of the winds' networks improves with all downsampling, i.e. they become more identifiable with respect to EEG ones. On the contrary, in the case of Forex' networks, the classification score drops to a minimum of 0.524 for  $\gamma \approx 95$ , corresponding to approximately one data point every 1.5 hours.

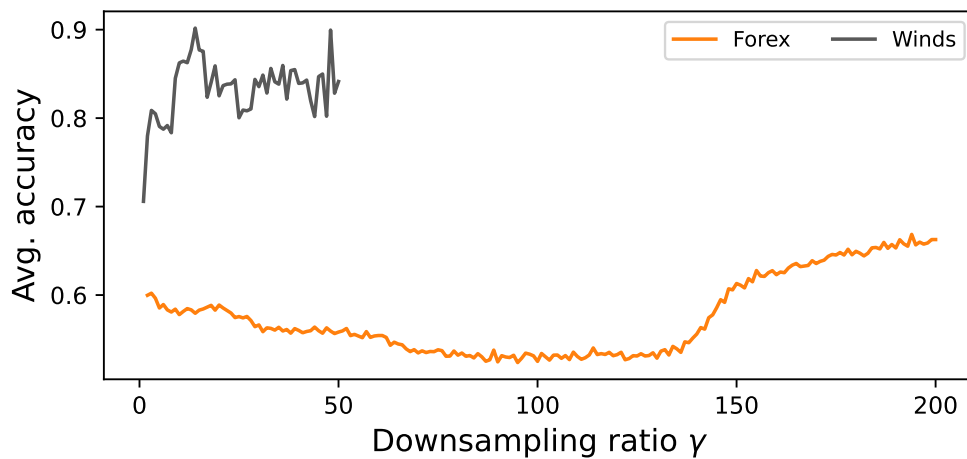


FIG. 10. Evolution of the classification score as a function of the downsampling applied to the original time series. Orange and grey lines respectively correspond to Forex and Winds functional networks. The left-most point, i.e.  $\gamma = 1$ , represent the value obtained with the original data.

### VIII. NETWORK DATA SET

With the aim of fostering future analyses on this topic, we provide the community with a public data set of functional networks. The file *FunctionalNetworks.zip* includes  $10^4$  unweighted networks, half of them representing the brain activity of control subjects, and the remainder the best optimisation obtained for Forex networks (i.e.  $l = 30$ ,  $\tau = 0.31$ , and  $\gamma = 95$ ). Files are text encoded, with each row representing a link, and with two tab-separated columns respectively reporting the source and destination nodes. Nodes are represented by integer numbers in range  $[0, 29]$ . An example of the structure is reported in Tab. XVII below.

TABLE XVII. Example of the content of the first network file, i.e. *Links\_EEG\_0000.txt*. Note that the first column (in italic) is only included here for reference, and is not actually contained in the file.

<i>Row number</i>	<b>Source node</b>	<b>Target node</b>
<i>1</i>	3	4
<i>2</i>	3	7
<i>3</i>	3	8
<i>4</i>	3	9
<i>5</i>	3	13
<i>6</i>	3	14
<i>7</i>	3	18
<i>8</i>	3	21
<i>9</i>	4	5
<i>10</i>	4	7
...	...	...

A graphical representation of two networks is presented in Fig. 11; note that the structure of both is qualitatively very similar, with a marked core-periphery configuration.

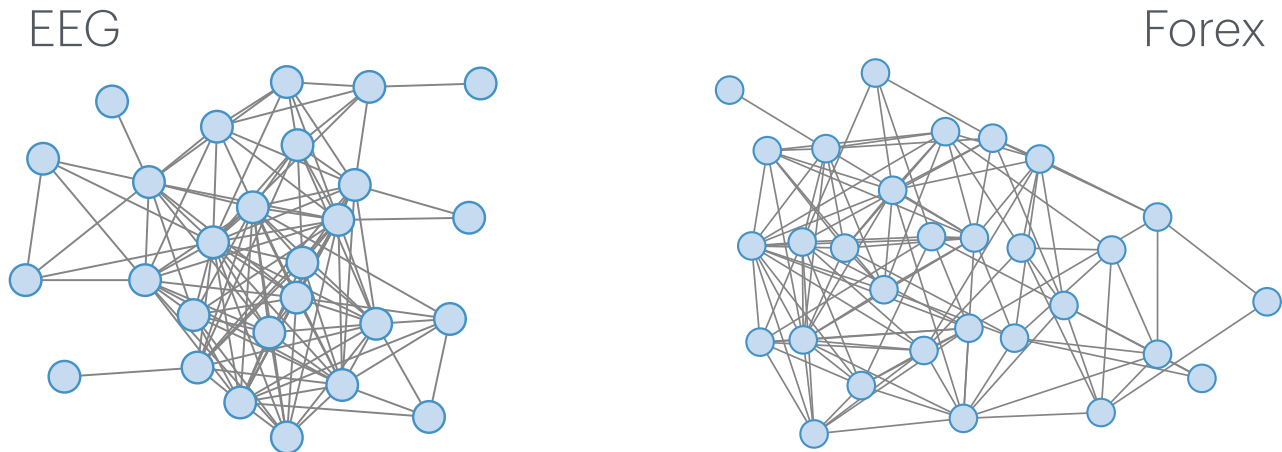


FIG. 11. Graphical representation of a brain functional network (left), and one Forex network (right), using the optimal reconstruction parameters for the latter ( $l = 30$ ,  $\tau = 0.31$ , and  $\gamma = 95$ ).

- 
- [1] E. Bullmore and O. Sporns, Complex brain networks: graph theoretical analysis of structural and functional systems, *Nature reviews neuroscience* **10**, 186 (2009).
- [2] H.-J. Park and K. Friston, Structural and functional brain networks: from connections to cognition, *Science* **342**, 1238411 (2013).
- [3] P. E. Vértes, R. M. Nicol, S. C. Chapman, N. W. Watkins, D. A. Robertson, and E. T. Bullmore, Topological isomorphisms of human brain and financial market networks, *Frontiers in Systems Neuroscience* **5**, 75 (2011).
- [4] M. Cristelli, *Complexity in financial markets: modeling psychological behavior in agent-based models and order book models* (Springer Science & Business Media, 2013).
- [5] K. L. Kirkland, High-tech brains: a history of technology-based analogies and models of nerve and brain function, *Perspectives in Biology and Medicine* **45**, 212 (2002).
- [6] R. L. Martensen, *The brain takes shape: An early history* (Oxford University Press, 2004).
- [7] D. D. Barney, *The network society*, Vol. 2 (Polity, 2004).
- [8] L. d. F. Costa, F. A. Rodrigues, G. Travieso, and P. R. Villas Boas, Characterization of complex networks: A survey of measurements, *Advances in physics* **56**, 167 (2007).
- [9] D. Papo, M. Zanin, J. A. Pineda-Pardo, S. Boccaletti, and J. M. Buldú, Functional brain networks: great expectations, hard times and the big leap forward, *Philosophical Transactions of the Royal Society B: Biological Sciences* **369**, 20130525 (2014).
- [10] K. Xu, W. Hu, J. Leskovec, and S. Jegelka, How powerful are graph neural networks? (2019), arXiv:1810.00826 [cs.LG].
- [11] M. Zanin and J. M. Buldú, Identifiability of complex networks, *Frontiers in Physics* **11**, 1290647 (2023).
- [12] H. L. Gallagher and C. D. Frith, Functional imaging of ‘theory of mind’, *Trends in cognitive sciences* **7**, 77 (2003).
- [13] C. Frith and U. Frith, Theory of mind, *Current biology* **15**, R644 (2005).
- [14] H. M. Wellman, *Making minds: How theory of mind develops* (Oxford University Press, 2014).
- [15] A. D. Nijhof, L. Bardi, M. Brass, and J. R. Wiersema, Brain activity for spontaneous and explicit mentalizing in adults with autism spectrum disorder: An fmri study, *NeuroImage: Clinical* **18**, 475 (2018).
- [16] C. W. Granger, Investigating causal relations by econometric models and cross-spectral methods, *Econometrica: journal of the Econometric Society*, 424 (1969).
- [17] T. Schreiber, Measuring information transfer, *Physical review letters* **85**, 461 (2000).
- [18] R. Vicente, M. Wibral, M. Lindner, and G. Pipa, Transfer entropy—a model-free measure of effective connectivity for the neurosciences, *Journal of computational neuroscience* **30**, 45 (2011).
- [19] A. Paszke, S. Gross, F. Massa, A. Lerer, J. Bradbury, G. Chanan, T. Killeen, Z. Lin, N. Gimelshein, L. Antiga, A. Desmaison, A. Kopf, E. Yang, Z. DeVito, M. Raison, A. Tejani, S. Chilamkurthy, B. Steiner, L. Fang, J. Bai, and S. Chintala, Pytorch: An imperative style, high-performance deep learning library, in *Advances in Neural Information Processing Systems*, Vol. 32, edited by H. Wallach, H. Larochelle, A. Beygelzimer, F. d'Alché-Buc, E. Fox, and R. Garnett (Curran Associates, Inc., 2019).
- [20] W. M. Organisation, *Technical Regulations, Volume II: Meteorological Service for International Air Navigation* (WMO, 2018 (updated in 2021)).
- [21] F. X. Diebold, *Elements of forecasting* (Citeseer, 1998).
- [22] M. Paluš, V. Komárek, Z. Hrnčíř, and K. Štěrbová, Synchronization as adjustment of information rates: Detection from bivariate time series, *Physical Review E* **63**, 046211 (2001).
- [23] B. G. Malkiel, Efficient market hypothesis, in *Finance* (Springer, 1989) pp. 127–134.
- [24] M. Sewell, The efficient market hypothesis: Empirical evidence, *International Journal of Statistics and Probability* **1**, 164 (2012).
- [25] M. Naseer and D. Y. Bin Tariq, The efficient market hypothesis: A critical review of the literature, *The IUP journal of financial risk management* **12**, 48 (2015).
- [26] R. Noldus and P. Van Mieghem, Assortativity in complex networks, *Journal of Complex Networks* **3**, 507 (2015).
- [27] M. Á. Serrano and M. Boguna, Clustering in complex networks. i. general formalism, *Physical Review E* **74**, 056114 (2006).
- [28] V. Latora and M. Marchiori, Efficient behavior of small-world networks, *Physical review letters* **87**, 198701 (2001).
- [29] M. E. Newman, Modularity and community structure in networks, *Proceedings of the national academy of sciences* **103**, 8577 (2006).
- [30] S. Fortunato, Community detection in graphs, *Physics reports* **486**, 75 (2010).
- [31] V. D. Blondel, J.-L. Guillaume, R. Lambiotte, and E. Lefebvre, Fast unfolding of communities in large networks, *Journal of statistical mechanics: theory and experiment* **2008**, P10008 (2008).
- [32] L. Li, D. Alderson, J. C. Doyle, and W. Willinger, Towards a theory of scale-free graphs: Definition, properties, and implications, *Internet Mathematics* **2**, 431 (2005).
- [33] M. Zanin, P. A. Sousa, and E. Menasalvas, Information content: Assessing meso-scale structures in complex networks, *Europhysics Letters* **106**, 30001 (2014).
- [34] L. Breiman, Random forests, *Machine learning* **45**, 5 (2001).
- [35] T. Koenig, D. Studer, D. Hubl, L. Melie, and W. Strik, Brain connectivity at different time-scales measured with eeg, *Philosophical Transactions of the Royal Society B: Biological Sciences* **360**, 1015 (2005).
- [36] S. J. Kiebel, J. Daunizeau, and K. J. Friston, A hierarchy of time-scales and the brain, *PLoS computational biology* **4**, e1000209 (2008).

- [37] R. Liégeois, J. Li, R. Kong, C. Orban, D. Van De Ville, T. Ge, M. R. Sabuncu, and B. T. Yeo, Resting brain dynamics at different timescales capture distinct aspects of human behavior, *Nature communications* **10**, 2317 (2019).
- [38] M. Golesorkhi, J. Gomez-Pilar, F. Zilio, N. Berberian, A. Wolff, M. C. Yagoub, and G. Northoff, The brain and its time: intrinsic neural timescales are key for input processing, *Communications biology* **4**, 970 (2021).